Journal of Inorganic Biochemistry 251 (2024) 112427

Contents lists available at ScienceDirect

Journal of Inorganic Biochemistry

journal homepage: www.elsevier.com/locate/jinorgbio

Cyclometalated iridium(III) complexes as anti-breast cancer and anti-metastasis agents *via* STAT3 inhibition

Yan Su [a,b,1], Jin Yang [b,1], Meng-Meng Wang [b], Hong-Bao Fang [b], Hong-Ke Liu [b], Zheng-Hong Yu [a,*], Zhi Su [b,*]

[a] Department of Rheumatology and Immunology, Jinling Hospital, Affiliated Hospital of Medical School, Nanjing University, Nanjing 210002, China
[b] Jiangsu Collaborative Innovation Center of Biomedical Functional Materials, College of Chemistry and Materials Science, Nanjing Normal University, Nanjing 210023, China

ARTICLE INFO

Keywords:
Iridium(III) complex
STAT3 inhibition
Anti-cancer
Anti-metastasis
Autophagy
Cell cycle arrest

ABSTRACT

Breast cancer is the most commonly diagnosed cancer and second-leading cause of cancer deaths in women. Signal transducer and activator of transcription 3 (STAT3) plays a critical role in promoting breast cancer cell proliferation, invasion, angiogenesis, and metastasis, and the high expression of STAT3 is related to the occurrence and poor chemotherapy sensitivity of breast cancer. Iridium(III) complexes **Ir-PTS-1**– **4** containing a pterostilbene-derived ligand were synthesized to inhibit the STAT3 pathway in breast cancer. **Ir-PTS-4** inhibited the proliferation of breast cancer cells by suppressing the expression of phosphorylated STAT3 and STAT3-related cyclin D1, arresting cell cycle in the S-phase, inducing DNA damage and reactive oxygen species (ROS) generation, eventually leading to autophagic cell death. The cell metastasis and invasion were also inhibited after **Ir-PTS-4** treatment. Besides, **Ir-PTS-4** exhibited excellent anti-proliferation activity in 3D multicellular tumor spheroids, showing potential for the treatment of solid tumors. This work presents the rational design of metal-based anticancer agents to block the STAT3 pathway for simultaneously inhibiting breast cancer proliferation and metastasis.

1. Introduction

Breast cancer (BC) is responsible for the majority of cancer-related deaths in women. Patients with primary breast cancer have a 5-year survival rate of 99%; however, the development of metastases reduces survival rates to 28% [1]. 20–30% of breast cancer cases metastasize to distant organs, accounting for 90% of breast cancer-related fatalities [2]. Great efforts are being made to develop targeted medicines to treat distinct types of BC [3]. Signal transducer and activator of transcription 3 (STAT3), a member of the cytoplasmic transcription factor family, transduces extracellular growth factor and cytokine signals and modulates the levels of genes related to cell cycle, angiogenesis, anti-apoptosis, and invasion/migration [4,5]. Abnormal STAT3 signaling is usually associated with tumor development and targeting the STAT3 protein may be a possible anti-tumor and anti-metastatic treatment strategy [6].

Metal complexes have stimulated researchers' interest because of their unique photochemical and photophysical properties and their potential as anticancer agents [7–9]. By interfering with STAT3, several metal complexes have been shown to suppress tumor development and metastasis. Leung et al. reported a series of cyclometalated rhodium(III) complexes as direct inhibitors of STAT dimerization [10]. Ma et al. designed a benzofuran-conjugated iridium(III) as an inhibitor of STAT3 activity in prostate cancer cells [11]. Rimoldi et al. synthesized Pt(II) complexes bearing 1,2,5-oxadiazole ligands which exhibited strong interaction with STAT3, leading to inhibition of STAT3 signaling pathway [12]. Gou et al. designed and prepared a series of Pt(II) complexes by conjugating four non-steroidal anti-inflammatory drugs (NSAIDs) derivatives with Pt(II) agents to inhibit metastasis and invasion of A2780 cells by suppressing the COX-2/JAK2/STAT3 axis [13]. Recently, Wang et al. reported two pterostilbene (PTS) modified Pt(IV) complexes SPP and DPP to combat BC *via* inhibiting the JAK-STAT3 pathway and regulating the tumor microenvironment [14]. The development of iridium complexes as potent anticancer agents has received increasing attention in recent years. On one hand, iridium complexes are widely used in biological imaging and biosensors because of their rich

* Corresponding authors.
E-mail addresses: 13327800182@189.cn (Z.-H. Yu), zhisu@njnu.edu.cn (Z. Su).
[1] Authors contributed equally.

https://doi.org/10.1016/j.jinorgbio.2023.112427
Received 17 October 2023; Received in revised form 6 November 2023; Accepted 11 November 2023
Available online 14 November 2023

photophysical properties, including high quantum yield, large Stokes shift, long fluorescence lifetime, good light stability, and strong cell penetration. On the other hand, diverse mechanisms of iridium complexes are exerted to inhibit the activities of cancer cells, including DNA binding [15–17], protein kinase activity inhibition [18,19] and so on. Until now, only one iridium-based STAT3 inhibitor has been reported, therefore, it is still urgently necessary to develop novel multifunctional anti-tumor agents that can both eradicate cancer cells and prevent metastasis.

As PTS has been previously reported as a STAT3 inhibitor [20], we hypothesized that the combination of the PTS-modified ligand with cyclometalated iridium(III) complex into a single molecular entity could potentially generate a metal-based inhibitor of STAT3 for the treatment of breast cancer. In this study, we designed and synthesized four PTS-derived ligand-conjugated cyclometalated iridium(III) complexes (**Ir-PTS-1**– **4**). **Ir-PTS-4** inhibited the proliferation of breast cancer cells by suppressing the expression of phosphorylated STAT3 and STAT3-related cyclin D1, arresting the cell cycle in the S-phase, inducing DNA damage and mitochondrial damage, eventually leading to autophagy. The cell metastasis and invasion were also inhibited after **Ir-PTS-4** treatment. Besides, **Ir-PTS-4** exhibited excellent anti-proliferation activity in 3D multicellular tumor spheroids, suggesting potential for the treatment of solid tumors. This work demonstrated the rational design of metal iridium-based anticancer agents to block the STAT3 pathway for simultaneously inhibiting tumor proliferation and metastasis in breast cancer treatment.

2. Experimental section

2.1. Materials and instrumentation

All the reagents were purchased from commercial sources and used without further purification unless stated otherwise. All the buffer components were of biological grade. Iridium (III) chloride hydrate ($IrCl_3$) was purchased from J&K Scientific. 1-hydroxybenzotriazole (HOBt), 2-phenylpyridine (ppy), 2-(thiophen-2-yl)pyridine (thpy), benzo[*h*]quinoline (dzq), 2-phenylquinoline (pq), NH_4PF_6, ethyl-bromacetat, pterostilbene (PTS), N-(3-Dimethylaminopropyl)-3-ethyl-carbodiimide hydrochloride (EDCI) and 3-(4,5-dimethylthiazol-2-yl)-2,5-diphenyltetrazolium bromide (MTT) were purchased from HEOWNS. Cisplatin was purchased from Energy Chemical. Dimethyl sulfoxide (DMSO) was purchased from Sigma Aldrich. Mito-tracker Green, Lyso-tracker Green, ER-tracker Green, Hoechst 33342, ROS assay kit and JC-1 assay kit were purchased from KeyGen Co. (China). Antibodies for western blot, such as STAT3, p-STAT3, LC3, GAPDH, RIP3, Bax, Bcl-2, Cytochrome c and γH_2AX were purchased from Abcam Co. (China). All the compounds tested were dissolved in DMSO just before the experiments and the final DMSO concentration was <1% (*v*/v).

The ^{1}H NMR spectra were recorded on a Bruker AVANCE 400 spectrometer at ambient temperature. UV–vis spectra were recorded on a LAMBDA 365 UV–vis spectrophotometer. The Electrospray ionization mass spectra (ESI-MS) were recorded on a LCQ system (Thermo Scientific). MTT data were recorded on a microplate reader (LabServ K3, Thermo Fisher Scientific, USA). Iridium contents in the samples were determined by ICP-MS (X Series 2, Thermo Fisher, USA). Cell imaging experiments were carried out on a confocal microscope (A1, Nikon, Japan). Flow cytometric analysis was done using a flow cytometer (BD FACSVerse, USA). Western blotting experiments were conducted on Mini-Protean Tetra System (BIO RAD, USA). The western blotting signal was enhanced by Tanon High-sig ECL Western Blotting Substrate and visualized by Tanon 5200 Multi.

2.2. Synthesis and characterization

Synthesis of the ligand (NˆN-PTS): pterostilbene (PTS)-derived ligand (E)-2-(4-(3,5-dimethoxystyryl) phenoxy) acetic acid and 4-aminomethyl-4-methyl-2,2-bipyridyl were prepared according to previously reported methods [21,22]. To a suspension of (E)-2-(4-(3,5-dimethoxystyryl) phenoxy) acetic acid (0.314 g, 1 mmol), EDCI (0.230 g, 1.2 mmol), HOBt (0.108 g, 0.8 mmol) in DMF, 4-aminomethyl-4-methyl-2,2-bipyridyl (0.239 g, 1.2 mmol) and 0.4 mL trimethylamine were added in a 50 mL Schlenk tube. The reaction mixture was stirred under argon atmosphere at ambient temperature for 48 h, then treated with ice-cold water and a deep rose white precipitate was filtered. The obtained solid was dissolved in CH_2Cl_2 and purified by column chromatography on silica gel eluted with CH_2Cl_2/CH_3OH. ^{1}H NMR (400 MHz, Chloroform-*d*) δ (ppm):δ 8.64 (dd, J = 5.0, 0.9 Hz, 1H), 8.55 (dd, J = 5.0, 0.8 Hz, 1H), 8.32 (dd, J = 1.7, 0.8 Hz, 1H), 8.24 (dt, J = 1.7, 0.9 Hz, 1H), 7.51–7.45 (m , 2H), 7.25 (dd, J = 5.0, 1.8 Hz, 1H), 7.18–6.89 (m, 6H), 6.67 (d, J = 2.3 Hz , 2H), 6.41 (t, J = 2.3 Hz, 1H), 4.72–4.60 (m, 4H), 3.85 (s, 6H), 2.46 (s, 3H)。.

Synthesis of the complexes **Ir-PTS-1**– **4**: $[Ir(ppy)_2Cl]_2$, $[Ir(thpy)_2Cl]_2$, $[Ir(dzq)_2Cl]_2$, and $[Ir(pq)_2Cl]_2$ were prepared according to previously reported methods. [23,24] A mixture of NˆN-PTS (0.25 mmol, 2 equiv) and iridium(III) chloro-bridged dimer (0.125 mmol, 1 equiv) was prepared in 45 mL CH_2Cl_2/CH_3OH (2:1, *v*/v) solvent by refluxing for 6 h under argon in the dark. After the mixture was cooled to room temperature, a 6-fold excess of NH_4PF_6 was added and stirred for another 2 h. The desired product was achieved after purification *via* column chromatography on silica gel eluted using CH_2Cl_2/CH_3OH.

Complex **Ir-PTS-1**: ^{1}H NMR (400 MHz, DMSO-d_6) δ (ppm):δ 8.84–8.62 (m, 3H), 8.26 (t, J = 8.2 Hz, 2H), 7.91 (dd, J = 10.4, 6.5 Hz, 4H), 7.74 (dd, J = 6.0, 2.8 Hz, 1H), 7.69 (t, J = 5.2 Hz, 1H), 7.61 (d, J = 5.9 Hz, 2H), 7.50 (dt, J = 12.0, 4.8 Hz, 3H), 7.23–7.10 (m, 4H), 7.06–6.96 (m, 3H), 6.95–6.85 (m, 3H), 6.70 (d, J = 2.1 Hz, 1H), 6.54–6.44 (m, 1H), 6.41–6.30 (m, 2H), 6.24–6.15 (m, 2H), 4.73–4.48 (m, 4H), 3.77 (d, J = 1.3 Hz, 3H), 2.53 (d, J = 4.6 Hz, 3H). ESI-MS (CH_3OH) calcd for:[**Ir-PTS-1**-PF_6^-]$^+$ *m/z* = 996.18, found m/z = 996.40. Elemental Analysis Calcd for $C_{52}H_{45}F_6IrN_5O_4P$: C, 54.73; H, 3.97; N, 6.14. Found: C, 54.98; H, 3.69; N, 6.04.

Complex **Ir-PTS-2**: ^{1}H NMR (400 MHz, DMSO-d_6) δ (ppm):δ 8.80 (dt, J = 15.1, 6.0 Hz, 1H), 8.69–8.62 (m, 2H), 7.84–7.68 (m, 6H), 7.66–7.62 (m, 3H), 7.59–7.49 (m, 5H), 7.22–7.12 (m, 2H), 7.02–6.88 (m, 5H), 6.71 (d, J = 2.3 Hz, 1H), 6.54–6.45 (m, 1H), 6.37 (d, J = 2.3 Hz, 1H), 6.17 (dd, J = 4.8, 2.5 Hz, 2H), 4.66 (s, 1H), 4.63–4.52 (m, 3H), 3.78 (s, 3H), 3.60 (s, 3H), 2.54 (d, J = 5.0 Hz, 3H). ESI-MS (CH_3OH) calcd for:[**Ir-PTS-2**-PF_6^-]$^+$ *m/z* = 1008.22, found m/z = 1008.20. Elemental Analysis Calcd for $C_{48}H_{41}F_6IrN_5O_4PS_2$: C, 49.99; H, 3.58; N, 6.07. Found: C, 50.05; H, 3.62; N, 5.98.

Complex **Ir-PTS-3**: ^{1}H NMR (400 MHz, DMSO-d_6) δ (ppm):δ 8.81–8.67 (m, 4H), 8.57 (ddt, J = 8.2, 6.2, 1.4 Hz, 2H), 8.08–8.05 (m, 2H), 7.97 (ddd, J = 8.9, 3.8, 2.5 Hz, 2H), 7.91–7.86 (m, 2H), 7.72 (dd, J = 5.7, 3.0 Hz, 1H), 7.67–7.57 (m, 4H), 7.56–7.48 (m, 3H), 7.44–7.36 (m, 2H), 7.18–7.14 (m, 3H), 6.99–6.95 (m, 1H), 6.89–6.86 (m, 1H), 6.68 (d, J = 2.3 Hz, 1H), 6.47 (d, J = 2.7 Hz, 1H), 6.35 (d, J = 2.3 Hz, 1H), 6.23–6.19 (m, 2H), 4.61 (s, 1H), 4.56 (d, J = 7.7 Hz, 3H), 3.76 (s, 3H), 3.58 (s, 3H). ESI-MS (CH_3OH) calcd for:[**Ir-PTS-3**-PF_6^-]$^+$ *m/z* = 1044.31, found m/z = 1044.30. Elemental Analysis Calcd for $C_{56}H_{45}F_6IrN_5O_4P$: C, 56.56; H, 3.81; N, 5.89. Found: C, 56.58; H, 3.89; N, 5.78.

Complex **Ir-PTS-4**: ^{1}H NMR (400 MHz, DMSO-d_6) δ (ppm):δ 8.72 (dt, J = 16.7, 6.0 Hz, 1H), 8.59–8.52 (m, 4H), 8.27 (t, J = 7.7 Hz, 4H), 7.98 (dd, J = 5.8, 2.8 Hz, 1H), 7.93 (dq, J = 8.5, 2.3 Hz, 3H), 7.54–7.47 (m, 2H), 7.46–7.39 (m, 3H), 7.27 (d, J = 8.8 Hz, 1H), 7.18–7.07 (m, 6H), 7.06–6.99 (m, 1H), 6.96–6.91 (m, 1H), 6.90–6.85 (m, 1H), 6.81 (tdt, J = 6.3, 3.2, 1.3 Hz, 2H), 6.70 (d, J = 2.3 Hz, 1H), 6.48 (d, J = 2.5 Hz, 1H), 6.42–6.31 (m, 4H), 4.67–4.55 (m, 2H), 4.49–4.40 (m, 2H), 3.78 (s, 3H), 3.60 (s, 3H), 2.38 (s, 3H). ESI-MS (CH_3OH) calcd for:[**Ir-PTS-4**-PF_6^-]$^+$ *m/z* = 1096.30, found m/z = 1096.40. Elemental Analysis Calcd for $C_{60}H_{49}F_6IrN_5O_4P$: C, 58.06; H, 3.98; N, 5.64. Found: C, 58.11; H, 4.02; N, 5.59.

2.3. UV–vis spectroscopy and fluorescence measurements

A LAMBDA 365 UV–vis spectrophotometer and a FS5 Spectrofluorometer were used with 1 cm path-length quartz cuvettes (3 mL). The stock solution of **Ir-PTS-1**, **Ir-PTS-2**, **Ir-PTS-3** and **Ir-PTS-4** in DMSO were prepared before measurements, and then diluted suitably with distilled water to the required concentration. The absorption spectra were recorded at ambient temperature unless otherwise stated. Fluorescence spectra were obtained by recording the emission spectra (from 450 to 800 nm) at ambient temperature (λ_{ex} = 405 nm).

2.4. Cell culture

MCF-7 and 4 T1 were obtained from the Experimental Animal Center of Sun Yat-Sen University (Guangzhou, China). MCF-10 A was purchased from Procell (CL-0525). MCF-7, 4 T1 and MCF-10 A were cultured in DMEM (Dulbecco's modified Eagle's medium, Gibco, USA) with 37 °C and 5% CO_2 supplemented with 10% inactivated fetal bovine serum (FBS) and 1% penicillin-streptomycin (Gibco, USA).

2.5. Cellular cytotoxicity assay

The cytotoxicity of the tested compounds towards cell lines was determined by MTT assay. Cells seeded in 96-well plates were incubated in a 5% CO_2 atmosphere in 100 μL of complete medium at 37 °C for 12 h. Then, 100 μL of freshly prepared culture medium containing drugs at different concentrations was added, and the mixture was incubated for an additional 48 h. 20 μL of MTT solution (5 mg/mL) was then added to each well, and the plates were incubated for an additional 4 h. Finally, the medium was removed, and DMSO (150 μL) was added. The absorbance at 570 nm was measured using a microplate reader (LabServ K3, Thermo Fisher Scientific, USA). Each well was triplicated to gain the mean values. IC_{50} values quoted are mean ± standard deviation (S.D.).

2.6. Assessment of lipophilicity

Briefly, **Ir-PTS-1**, **Ir-PTS-2**, **Ir-PTS-3** and **Ir-PTS-4** were added to the mixture of octanol/NaCl aqueous solution (1:1, *v*/v), respectively. The mixture was shaken at 25 °C, 600 rpm for 48 h to achieve partitioning equilibrium between octanol and aqueous NaCl. The oil phase and the water phase were then separated by centrifugation (3000 rpm, 10 min) and collected. The concentration of the solute was determined by UV–vis absorbance. The lipo-hydro partition coefficient log $P_{o/w}$ ($P_{o/w} = C_o/C_w = A_o/A_w$, A stands for absorbance) were calculated.

2.7. Intracellular localization study

MCF-7 cells were seeded into 35 mm confocal dishes for 12 h at 37 °C and then incubated for 2 h after adding **Ir-PTS-4** (4 μM). Upon completion, cells were washed twice with PBS and incubated with Mito-Tracker Green, Lyso-Tracker Green, ER-Tracker Green, or Hoechst 33342 fluorescent probes at 37 °C, respectively. Cells were finally washed with PBS and imaged by confocal microscopy under a 100 × oil-immersion objective lens. The excitation wavelength for **Ir-PTS-4** and Hoechst 33342 were set at 405 nm and 352 nm, respectively. And the emission wavelength for **Ir-PTS-4** and Hoechst 33342 were set at 600 ± 20 nm and 460 ± 20 nm, respectively. The excitation wavelength for Mito-tracker Green, Lyso-tracker Green and ER-tracker Green were set at 488 nm. The emission wavelength for Mito-tracker Green, Lyso-tracker Green and ER-tracker Green were set at 520 ± 20 nm.

2.8. Intracellular distribution study

The cellular distribution of **Ir-PTS-4** in MCF-7 cells was determined by measuring the iridium contents. Briefly, cells were seeded and incubated overnight under standard growth conditions. The culture medium was removed and replaced with fresh medium/DMSO (*v*/v, 99:1) containing complex **Ir-PTS-4** (4 μM). After incubation for 6 h, the cells were harvested with trypsin, washed with PBS and counted. Cell pellets were lysed in RIPA Lysis Buffer (Beyotime Biotechnology, China) and the nucleus and mitochondria fractions were extracted using the Mitochondria/Nuclei Isolation Kit (KeyGEN, China) according to the manufacturer's instructions. These fractions in the stock buffer were then digested with concentrated nitric acid (100 μL) at 95 °C for 2 h, hydrogen peroxide (30%, 50 μL) at 95 °C for 1.5 h, and concentrated hydrochloric acid (50 μL) at 95 °C for 1.5 h to give fully homogenized solutions. Finally, the solutions were diluted with water to a final volume of 2 mL for the measurement and iridium contents in the samples were determined by ICP-MS (X Series 2, Thermo Fisher, USA). The average of three parallel experimental data was reported.

2.9. Detection of intracellular Ca^{2+}

The MCF-7 cells were seeded into a 35 mm dish and incubated at 37 °C for 24 h. After that, the cells were then incubated with fresh DMEM containing **Ir-PTS-4** at different concentrations. After removing the culture medium, cells were stained with Fluo-4 AM fluorescent probes. Finally, intracellular calcium ions were detected using confocal microscopy.

2.10. Lysosomal damage assay

MCF-7 cells were seeded into a 35 mm dish and cultured for 24 h. After that, the cells were treated with **Ir-PTS-4** for 24 h, and washed with PBS three times. Before being imaged, the cells were incubated with AO (5 μM) for another 0.5 h, The excitation wavelength of AO was 488 nm, and the capture emission region was 515–545 nm for the green channel and 610–640 nm for the red channel.

2.11. Intracellular ROS level analysis

2′,7′-dichlorofluoresecein diacetate (H_2DCHF-DA) was used to measure the reactive oxygen species (ROS) accumulation. For the flow cytometry analysis of cellular ROS, MCF-7 cells in the logarithmic phase were harvested and placed (3×10^5 cells/well) into a 6-well plate at the incubator for 12 h, the cell was treated for 24 h with **Ir-PTS-4**. The cells were dyed with H_2DCHF-DA for 30 min, then the cell samples were analyzed after washing with culture medium without FBS and analyzed using a BD FACSVerse flow cytometer with excitation at 488 nm and emission at 530 ± 30 nm. Data were analyzed using FlowJo 7.6.1 software. 10, 000 cells were acquired for each sample.

For the confocal microscopy analysis of cellular ROS, MCF-7 cells were seeded into 35 mm confocal dishes (JET BIOFIL, Canada). After being cultured overnight, the cells were treated with the complex for 24 h, after being stained with H_2DCHF-DA probe and washed twice with serum-free medium, the cells were immediately observed by confocal microscopy (A1, Nikon, Japan) with excitation at 488 nm and emission at 530 ± 20 nm.

2.12. Mitochondrial membrane potential (MMP) detection

The mitochondrial membrane potential was determined by using JC-1 dye. For the flow cytometry analysis of MMP, MCF-7 cells were seeded (3×10^5 cells/well) in a 6-well cell-culture plate for 12 h. The cells were treated with **Ir-PTS-4** for 24 h in an incubator at 37 °C. Then the cells were harvested with 0.25% trypsin, and washed with PBS three times. After the incubation of 0.5 mL JC-1 working solution for 30 min, the cell samples were washed with 1 × incubation buffer and analyzed by using a BD FACSVerse flow cytometer.

For the confocal microscopy analysis of MMP, MCF-7 cells were seeded into 35 mm confocal dishes (JET BIOFIL, Canada). After cultured overnight, the cells were treated with the complex for 24 h at 37 °C.

After being stained with JC-1 working solution for 30 min, the cells were washed with incubation buffer and then immediately observed by confocal microscopy (A1, Nikon, Japan).

2.13. Cell cycle analysis

The cell cycle analysis was conducted as the manufacturer's protocol. MCF-7 cells were cultured in 6-well plates and incubated with **Ir-PTS-4** for 24 h. Cells were collected and fixed with 70% ethanol. After storage at 4 °C overnight, cells were centrifuged and washed three times with cold PBS and resuspended in a 500 μL PBS buffer containing PI and RNase A (9:1) for 30 min in the dark. The samples were analyzed by a BD FACSVerse flow cytometer and the data were processed using FlowJo 7.6.1 software.

2.14. Wound healing assay

MCF-7 cells were seeded in 6-well plates at 10×10^4 cells per well. The cells were allowed to adhere to the surface, and once they reached 80% confluence, the monolayer was wounded using a 200-μl pipette tip to streak each hole vertically. The cells were washed with PBS three times and incubated in serum-free DMEM for another 24 h. Images of the scratches were captured with a microscope camera. Data were collected from three independent experiments. The percentage of wound healing was calculated using the following formula: [1- (empty area 12 (24) h/ empty area 0 h)] × 100.

2.15. Transwell migration assay

Transwell chambers with 8-μm pores (Corning, NY) were used to evaluate the migration of MCF-7 cells. The upper chamber was filled with 5×10^4 cells from each sample in serum-free medium for migration analysis. After incubating the cells at 37 °C for 24 h, the cells migrating to the bottom of the filter were incubated with 0.5% crystal violet at room temperature for 20 min. For quantitative measurement, five areas (at ×100 magnification) were randomly selected under an optical microscope, and the cells were counted.

2.16. Western blot analysis

MCF-7 cells were seeded in 10 cm dishes for 12 h, then treated with the **Ir-PTS-4** (4 μM) for 24 h. After that, the harvested cells were lysed by RIPA lysis buffer. The protein concentration was quantified using the BCA Quantitation Kit. Equal amounts of cellular lysate (20 μg) were separated on SDS polyacrylamide gel electrophoresis and then transferred to polyvinylidene difluoride (PVDF) membranes (Millipore, MA, USA). Membranes were blocked in QuickBlock™ Blocking Buffer, and then incubated overnight with the primary antibodies at 4 °C. After a subsequent washing step, the membrane was incubated with the appropriate horseradish peroxidase conjugated secondary antibody. Images were captured using Tanon High-sig ECL Western Blotting Substrate and Tanon 5200 Multi, and analyzed manually with Image J software.

2.17. 3D tumor spheroids viability assays

The multicellular tumor spheroids (MCTSs) were prepared with MCF-7 cells by seeding 2500 cells/well in an Ultra-Low Attachment 96-well plate (Corning). The spheroids were incubated for 1 day. The diameter of the MCF-7 MCTSs proved to be around 500 μm after 1 day. The spheroid growth was monitored using a live-cell phase-contrast microscope (Axio Observer, Zeiss). After 5 d incubation, the spheroids were washed twice with PBS, stained with Calcein AM/PI following the manufacturer's instructions (Beyotime, China), and fixed in 4% paraformaldehyde. Spheroids were placed in a glass-bottom dish and imaged at different depths (z-stacking) with a confocal scanning microscopy system (Calcein AM: $\lambda_{ex} = 488$ nm and λ_{em} range 500–550 nm, PI: $\lambda_{ex} =$ 561 nm and λex range 570–620 nm).

2.18. Statistical analysis

All biological experiments were performed in triplicate and each experiment was repeated at least twice. The quantitative data are presented as means ± standard deviations (SD). Statistical significance was performed using an unpaired two-tailed Student's *t*-test. Statistical significance was set at $^*P < 0.05$, and extreme significance was set at $^{**}P < 0.01$, and $^{***}P < 0.001$.

3. Results and discussion

3.1. Synthesis and characterization

The modified NˆN-PTS ligand was synthesized from 4-aminomethyl-4-methyl-2,2-bipyridyl with pterostilbene (PTS)-derived ligand (E)-2-(4-(3,5-dimethoxystyryl) phenoxy) acetic acid [25,26]. Complexes [Ir(C—N)$_2$(NˆN-PTS)](PF$_6$) [C-*N* = 2-phenylpyridine (ppy, **Ir-PTS-1**), 2-(2-thienyl)pyridine (thpy, **Ir-PTS-2**), benzo[*h*]quinoline (dzq, **Ir-PTS-3**) 2-phenylquinoline (pq, **Ir-PTS-4**)] containing NˆN-PTS as ligand were prepared according to literature methods (Fig. 1, Scheme S1) [26]. The structures of **Ir-PTS-1**– **4** were fully characterized by ^{1}H nuclear magnetic resonance (NMR) spectroscopy and electrospray ionization-mass spectrometry (ESI-MS) (Figs. S1-S9). The photophysical properties of complexes were first studied (Fig. S10). Complexes **Ir-PTS-1**– **4** exhibit similar absorption spectra in the range of 250–550 nm. Moreover, the emission intensity of **Ir-PTS-4** was about 6-fold stronger than that of **Ir-PTS-1/2**, which was excited at 405 nm. This finding indicated that **Ir-PTS-4** showed better photophysical properties and could be favorable for cell imaging. Lipophilicity (log $P_{o/w}$) has a significant impact on drug cellular uptake, distribution, and cytotoxicity [27]. The shaking flask method was used to determine the lipophilicity of four complexes. The log $P_{o/w}$ values for complexes **Ir-PTS-1**– **4** were determined to be 1.48, 1.06, 1.49, and 1.32, respectively (Table S1). This implied that the four complexes exhibited higher lipophilicity, which could help them permeate the lipid bilayer of the cell membrane.

3.2. In vitro anticancer activity

The cytotoxicity of complexes **Ir-PTS-1**– **4** was tested against breast cancer cell lines (MCF-7 and 4 T1) and normal breast cell line (MCF-10 A) by a MTT assay [28], with ligand PTS, NˆN-PTS and cisplatin as the reference. The half-maximal inhibitory concentrations (IC_{50} values) obtained after 48 h of drug treatment are listed in Table 1. The ligand PTS and NˆN-PTS showed almost no toxicity against the tested cell lines. **Ir-PTS-1**– **4** exhibited strong anti-proliferative activity, with the following order: **Ir-PTS-4** > **Ir-PTS-1** > **Ir-PTS-2** > **Ir-PTS-3**. **Ir-PTS-4**,

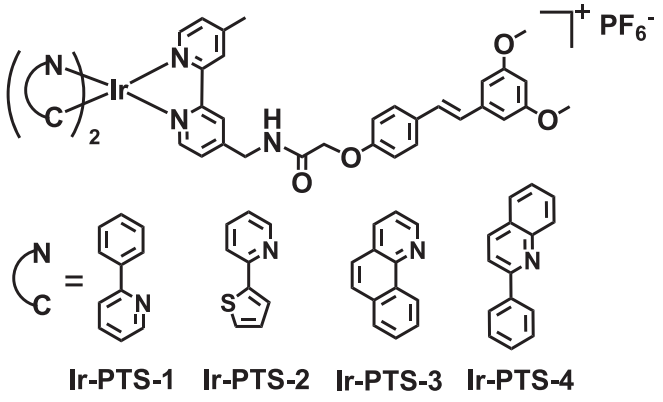

Fig. 1. Chemical structures of complexes **Ir-PTS-1**– **4.**

Table 1
IC_{50} values (μM) of tested compounds towards different cell lines. Data are presented as means ± standard deviations obtained in at least three independent experiments and the treatment period was 48 h.

Compounds	MCF-7	4 T1	MCF-10 A
PTS	>100	>100	>100
N^N-PTS	>100	>100	>100
Ir-PTS-1	4.1 ± 0.1	3.3 ± 0.2	3.7 ± 0.3
Ir-PTS-2	4.6 ± 0.3	5.6 ± 0.1	5.4 ± 0.4
Ir-PTS-3	4.7 ± 0.1	5.1 ± 0.6	11.5 ± 0.1
Ir-PTS-4	1.9 ± 0.1	3.6 ± 0.1	6.5 ± 0.1
Cisplatin	4.3 ± 0.1	9.6 ± 0.2	10.8 ± 1.2

with an IC_{50} value of 1.9 μM to MCF-7 cells, is the most potent among all compounds. Notably, the toxicity of **Ir-PTS-4** to normal cells was reduced by about 3.4-fold, showing better cell selectivity compared with **Ir-PTS-1**– **3** and cisplatin. Based on the cytotoxic profile, we chose **Ir-PTS-4** as the targeting compound for further mechanism investigation.

3.3. Cellular accumulation

Due to the excellent photophysical properties of Ir(III) complexes, the accumulation of **Ir-PTS-4** in MCF-7 cells was detected by confocal laser scanning microscopy (CLSM) and flow cytometer. As shown in Fig. 2, an increased red fluorescence intensity in MCF-7 cells was observed, suggesting the uptake of **Ir-PTS-4** was highly dependent on the concentration and the incubation time. We further examined the cellular uptake mechanisms of **Ir-PTS-4** by assessing the influence of incubation temperature (37 °C and 4 °C), metabolic inhibitor (2-deoxy-D-glucose and oligomycin) and endocytic inhibitor (NH_4Cl) on the cellular uptake level of **Ir-PTS-4**. As shown in Fig. S11, compared with that at 37 °C, the fluorescence intensity of **Ir-PTS-4** in MCF-7 cells was markedly reduced on incubation at 4 °C or pretreatment with metabolic inhibitor. Meanwhile, the cellular uptake efficiency is barely affected by pretreated with NH_4Cl. These results demonstrated that **Ir-PTS-4** penetrated the cell membrane primarily through an energy-dependent mechanism instead of endocytic pathways.

3.4. Subcellular localization

Studies on cellular localization of phosphorescent metal complexes may offer more clues for the study of anticancer mechanisms [29]. The cellular localization of the **Ir-PTS-4** in MCF-7 cells was investigated by co-localization staining with commercial dyes Lyso-Tracker Green, Mito-Tracker Green, endoplasmic reticulum (ER)-Tracker Green and Hoechst 33342. The Pearson's correlation coefficients (PCCs) of complex **Ir-PTS-4** were 0.55, 0.53, 0.54 and 0.08 with ER-Tracker Green, Mito-Tracker Green, Lyso-Tracker Green and Hoechst 33342, respectively (Fig. 3a). These results revealed that **Ir-PTS-4** localized in the ER, mitochondria and lysosome of MCF-7 cells. To further assess the intracellular distribution of **Ir-PTS-4**, the iridium content of MCF-7 cells was quantified by inductively coupled plasma-mass spectrometry (ICP-MS). As shown in Fig. S12, there were about 65% and 32% of iridium were localized in the cytosol and mitochondria in the **Ir-PTS-4**-treated MCF-7 cells, respectively. These data displayed that **Ir-PTS-4** are primarily distributed in mitochondria, lysosome and ER.

3.5. Induction of Ca^{2+} overload and lysosomal membrane permeabilization

According to previous studies, the ER is highly sensitive to Ca^{2+} concentration turbulence [30–32]. Fluo-4 AM can be hydro-lysed by the esterase enzymes to Fluo-4 which can bind to free Ca^{2+}, and turn fluorescent [33]. Therefore, in order to depict the efflux of Ca^{2+} induced by **Ir-PTS-4** *via* ER stress, Fluo-4 AM was used as an "OFF-ON" probe for intracellular Ca^{2+}. As shown in Fig. 3b, the fluorescence intensity was significantly increased in a dose-dependent manner after treatment with **Ir-PTS-4**, which suggested an increased intracellular Ca^{2+} level. While MCF-7 cells in the control group did not show this phenomenon, suggesting that **Ir-PTS-4** could induce the efflux of Ca^{2+} from the ER.

Due to the accumulation of complex **Ir-PTS-4** in the lysosome, we further detected whether **Ir-PTS-4** could induce lysosomal membrane permeabilization (LMP) by acridine orange (AO) staining. As shown in Fig. 3c, MCF-7 cells incubated with **Ir-PTS-4** showed obvious green fluorescence of lysosomes as the control, whereas the red fluorescence intensity in the **Ir-PTS-4**-treated MCF-7 cells was significantly attenuated, suggesting the occurrence of LMP.

3.6. Mitochondrial dysfunction

Since **Ir-PTS-4** could accumulate in the mitochondria of MCF-7 cells, the impacts on mitochondrial functionality were then studied. Mitochondria is the main organelle for reactive oxygen species (ROS) production and ROS elevation could cause mitochondrial damage [34].

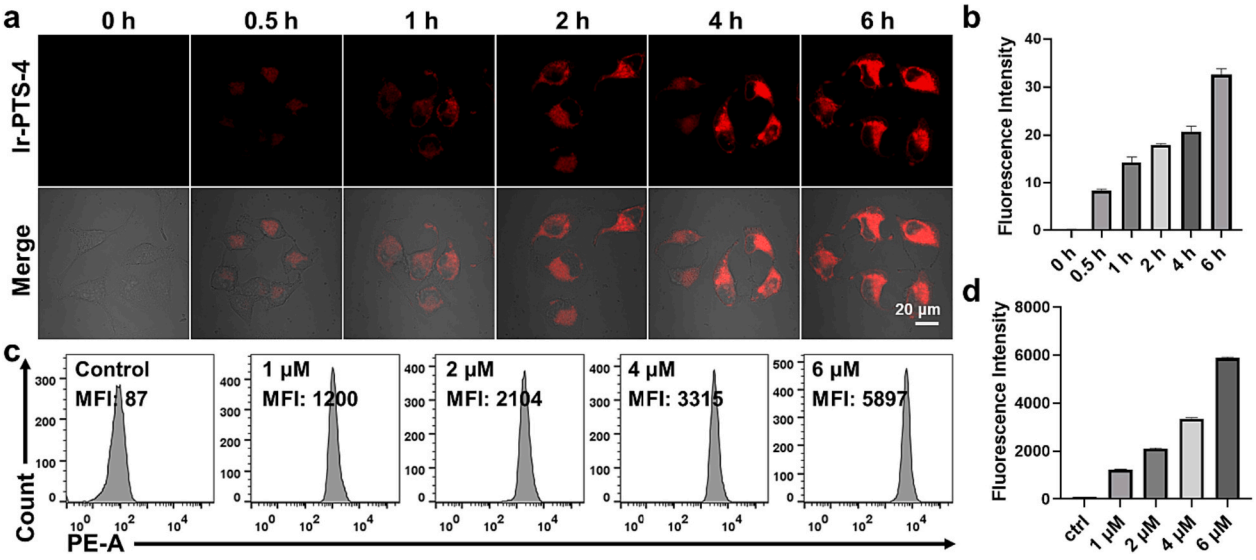

Fig. 2. (a) Temporal profiles of confocal imaging and (b) quantification analysis, and (c) dose-dependent profiles of flow cytometry results and (d) quantification analysis of cellular uptake of **Ir-PTS-4** in MCF-7 cells. Scale bar: 20 μm.

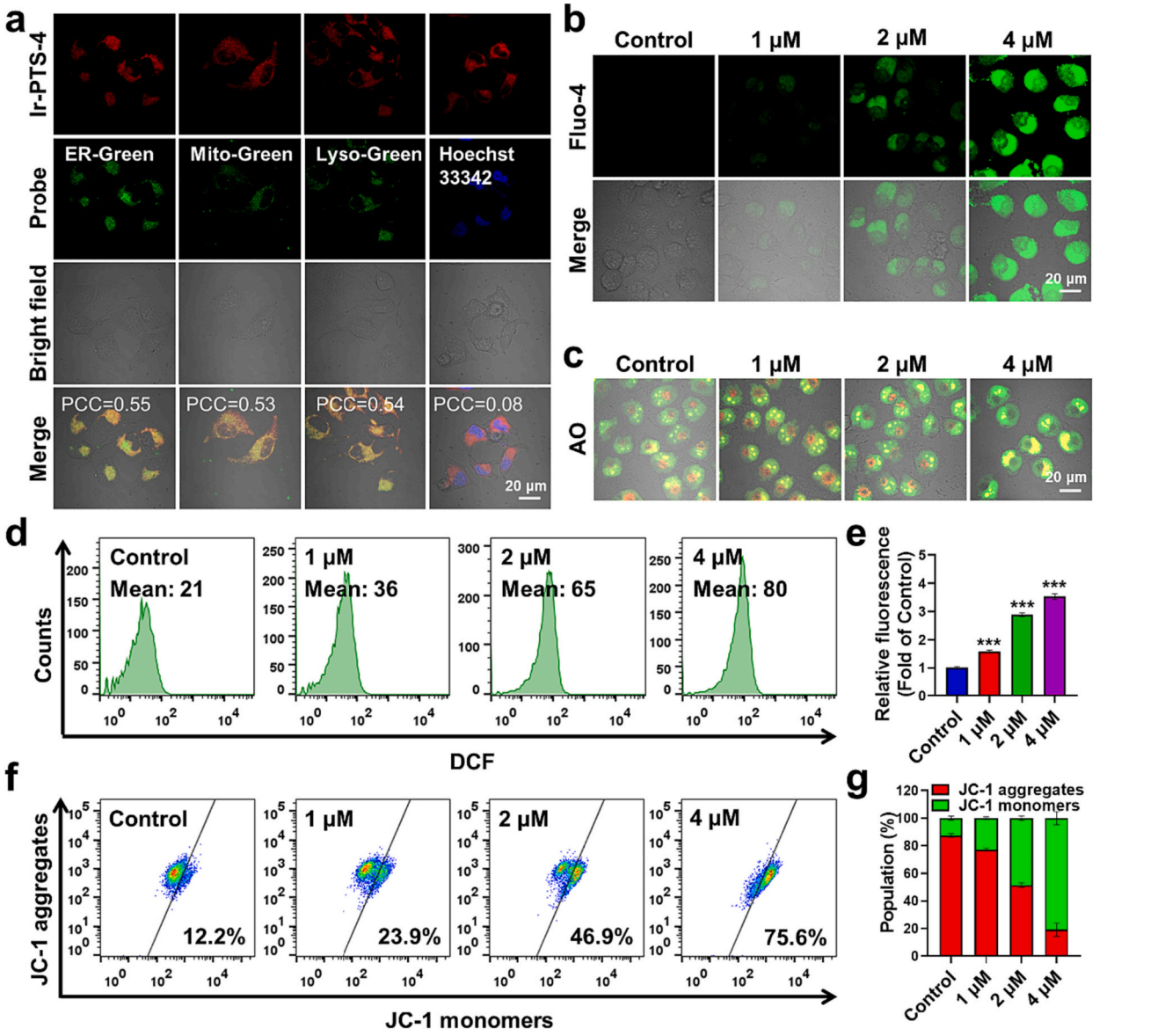

Fig. 3. (a) Subcellular distribution confocal study of **Ir-PTS-4** in MCF-7 cells by co-localization imaging. The cells were co-stained with Mito-Tracker Green (200 nM) or Lyso-Tracker Green (50 nM), or ER-Tracker Green (1 μM), or Hoechst 33342 (10 μg/mL). (b) Confocal images of intracellular Ca^{2+} assays with Fluo-4 AM in MCF-7 cells for 24 h. (c) AO staining for LMP analysis in MCF-7 cells. (d-e) Flow cytometry quantification of the ROS generation and (f-g) flow cytometry results of a JC-1 assay in MCF-7 cells after treatment with **Ir-PTS-4**, respectively, for 24 h. Scale bar: 20 μm. (For interpretation of the references to colour in this figure legend, the reader is referred to the web version of this article.)

Intracellular ROS levels were determined by flow cytometry using a ROS probe, 2′,7′-dichlorofluorescein diacetate (H_2DCF-DA). H_2DCF-DA will be oxidized to highly fluorescent 2′,7′-dichlorofluorescein (DCF) by a wide range of cellular ROS [35]. As shown in Fig. 3d-e, after treatment with **Ir-PTS-4** for 24 h, a dramatic dose-dependent increase in DCF fluorescence intensity was observed in MCF-7 cells, indicating the generation of ROS. An approximately 3.5-fold increase in DCF fluorescence intensity was observed in cells treated with **Ir-PTS-4** (4 μM). Meanwhile, CLSM images indicated a concentration-dependent elevation of ROS generation in MCF-7 cells was observed after **Ir-PTS-4** the treatment (Fig. S13a).

The effects on the mitochondrial membrane potential (MMP) were evaluated using the JC-1 assay kit [36]. The changes in MMP were reflected by the increase of JC-1 monomers (green fluorescence) and decrease of JC-1 aggregate (red fluorescence). As shown in Fig. 3e-f, in comparison with the control, a significant dose-dependent loss of MMP s was observed in **Ir-PTS-4**-treated MCF-7 cells, dropping from 12.2% to 75.6%. CLSM analysis was also performed to detect the MMP in MCF-7 cells. **Ir-PTS-4**-treated MCF-7 cells emitted strong green fluorescence (Fig. S13b), thus suggesting that **Ir-PTS-4** has a strong ability to impair the MMP. These results indicated that **Ir-PTS-4** could induce ROS elevation and loss of MMP.

3.7. Cell death mechanism study

Many studies have shown that damage to mitochondrial and lysosomal can lead to autophagy [37,38]. LC3 (microtubule-associated with protein light chain 3) is a common molecular marker of autophagy [39]. During autophagy, LC3-I (cytoplasmic type I) is hydrolyzed by enzymes to cut off a polypeptide and produce LC3-II (type II LC3) located in the membrane of autophagic cells. The marker of autophagy is the conversion of LC3 protein from type I to type II [40]. From the results of the western blot experiment, the ratio of LC3-II to LC3-I increased significantly after treatment with **Ir-PTS-4**, compared to the control (Fig. 4a

and c). All these data collectively suggest that **Ir-PTS-4** can induce autophagy in MCF-7 cells.

We further investigated the apoptosis of MCF-7 cells induced by **Ir-PTS-4** by flow cytometry after annexin V-FITC and propidium iodide (PI) double staining. As shown in Fig. S14, flow cytometry analysis indicated that there is no distinct dose-dependent increase of the apoptotic MCF-7 cells. The expressions of apoptosis-related proteins Bax (proapoptotic protein), Bcl-2 (anti-apoptotic protein), cytochrome *c* and necrosis marker RIP3 (receptor-interacting kinase protein 3) were not changed in **Ir-PTS-4**-treated MCF-7 cells as compared with that of the control. These data suggested that the cell death mediated by **Ir-PTS-4** occurred *via* a non-apoptotic/necrotic pathway but autophagic pathways.

3.8. Inhibition of STAT3 and cell cycle arrest

Recent clinical and preclinical findings suggest overexpressed and constitutively activated STAT3 is involved in the progression, proliferation, and metastasis of breast cancer [41], the mechanism of action of **Ir-PTS-4** on STAT3 signaling was further explored in MCF-7 cells by immunoblotting. As shown in Fig. 4b-c, **Ir-PTS-4** reduced the expression of phosphorylated STAT3 (p-STAT3) in a dose-dependent manner relative to the control, while the expression of STAT3 was only slightly affected. The results indicated that **Ir-PTS-4** selectively decreased the level of p-STAT3, which was not due to a constitutional decrease in total STAT3 expression.

It has been reported that STAT3 can upregulate cyclin D1 to promote the proliferation of breast cancer cells, indicating a potential involvement of STAT3 in the cell cycle [42]. The cyclin D1 expression and the cell cycle distribution of MCF-7 cells were analyzed after exposure to **Ir-PTS-4** for 24 h. As shown in Fig. 4b-d, **Ir-PTS-4** induced a significant downregulation of cyclin D1 and arrested cell cycle in the S phase (24.8%) as compared with the control (14.5%). Cell cycle arrest could induce cellular DNA damage. Then, the expression of γ-H2AX in MCF-7 cells was determined by western blotting, which is a biomarker of DNA damage [14]. As shown in Fig. 4b-c, a concentration-dependent increase in the expression of γ-H2AX was observed in MCf-7 cells, indicating that **Ir-PTS-4** could induce DNA damage. Thus, we concluded that the anticancer mechanism for **Ir-PTS-4** towards MCF-7 cells involved STAT3 inhibition and cell cycle arrest.

3.9. Inhibition of cell migration and invasion

Migration is a key step in cancer progression, and emerging evidence indicated that aberrantly elevated STAT3 is one of the key driving factors of cancer metastasis and invasiveness [43]. Hence, the anti-migration activity of **Ir-PTS-4** was tested by a wound healing assay and a transwell assay. As shown in Fig. 5a and c, the wound closure ratio of **Ir-PTS-4**-treated MCF-7 cells was only 11.3%, in contrast to 75.9% of the control group after 24 h incubation. As shown in Fig. 5b, the number of cells migrating through pores was significantly decreased by **Ir-PTS-4** in a dose-dependent manner in MCF-7 cells. Migration cells treated with **Ir-PTS-4** (2 μM) were observed in only 14.7% of the chamber compared to the control group (Fig. 5d). These results suggested that **Ir-PTS-4** could effectively inhibit cell migration and invasion.

3.10. Biological evaluation on 3D multicellular tumor spheroids

3D multicellular tumor spheroids (MCTSs) with the tumor microenvironments of intercellular and cell-extra-cellular matrix interactions have been used to mimic the solid tumor *in vitro* [44]. As shown in Fig. 6a, the control spheroids grew to a diameter of around 600 μm after 5 days of incubation, which demonstrated the great proliferation capacity of MCF-7 spheroids. The diameter shrank to only 350 μm after 5 days of incubation with **Ir-PTS-4** (10 μM). In addition, a Calcein AM/PI double staining was examined to further illustrate the anti-proliferation performance. Calcein AM only enters into live cells and emits green fluorescence, whereas PI only enters into dead cells with red fluorescence under irradiation. As shown in Fig. 6b, the untreated control MCTSs exhibited a bright green fluorescence signal indicating that the cells were alive. However, the MCTSs treated with **Ir-PTS-4** showed weak green fluorescence as well as strong red fluorescence, indicating the superior capacity of **Ir-PTS-4** to inhibit cell growth and induce cell death of 3D MCTSs.

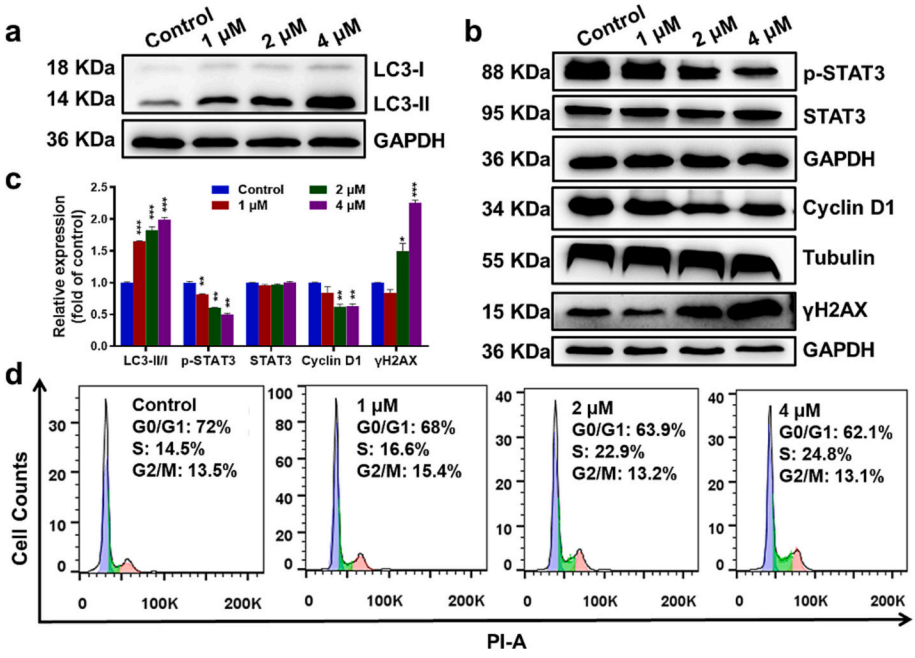

Fig. 4. (a and b) Immunoblotting of LC3-I/II, p-STAT3, STAT3, Cyclin D1 and γH2AX in MCF-7 cells treated with **Ir-PTS-4** for 24 h. (c) Quantitative analysis of immunoblotting in a-b. (d) Flow cytometry results of cell cycle distribution in MCF-7 cells after treatment with **Ir-PTS-4** for 24 h.

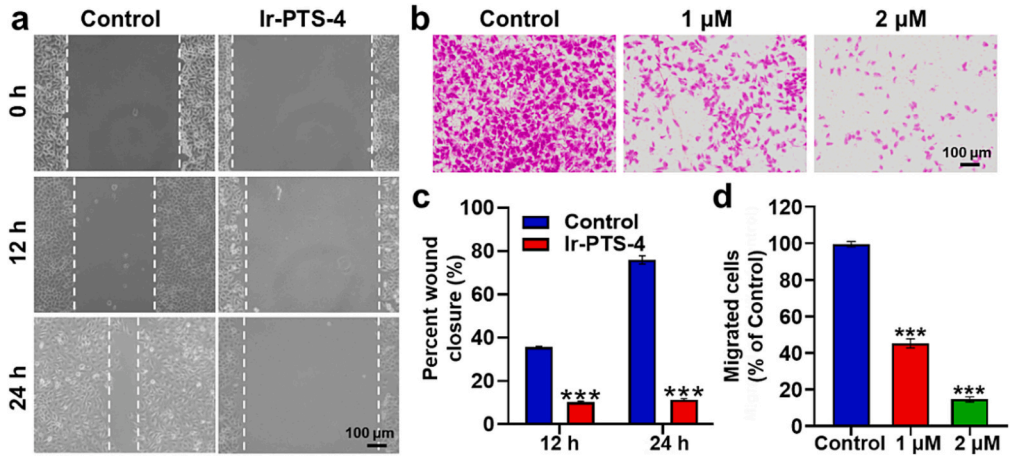

Fig. 5. (a) Wound-healing assay of MCF-7 cells after incubation with **Ir-PTS-4** and (c) the percent wound closure was calculated. (b) Representative images of MCF-7 cells were observed by transwell invasion assay and (d) the number of migrated cells was counted. Scale bar: 100 μm.

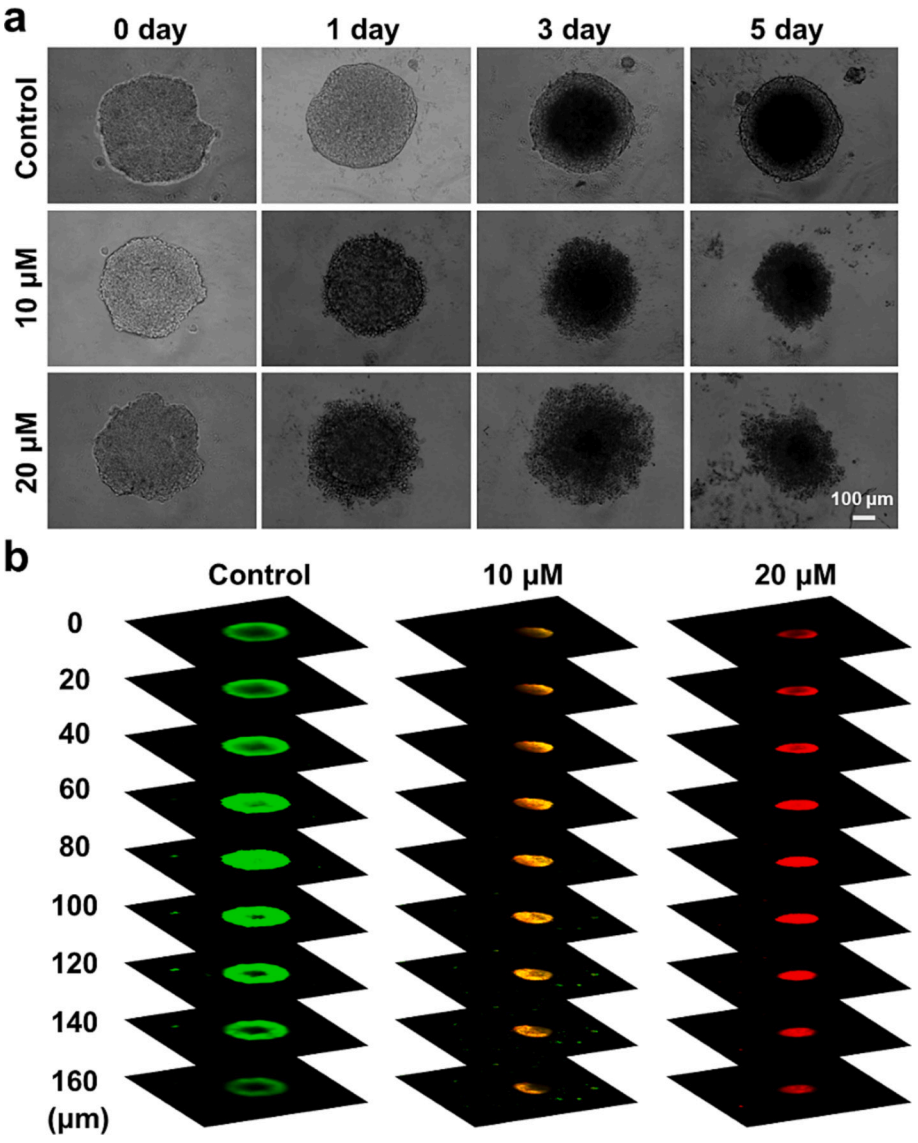

Fig. 6. (a) Representative images of 3D MCF-7 tumor spheroids after being treated with **Ir-PTS-4**. (b) Images of MCF-7 3D MCTSs treated with **Ir-PTS-4** for 5 days, and stained with Calcein AM/PI for the live/dead cells. Scale bar: 100 μm.

4. Conclusion

In conclusion, we have developed four PTS-derived ligand conjugated cyclometalated iridium(III) complexes **Ir-PTS-1**– **4** to combat breast cancer cells *via* inhibiting STAT3 signaling pathway. All four complexes exhibit higher cytotoxicity towards breast cancer cells, especially **Ir-PTS-4**. Besides, **Ir-PTS-4** could increase the intracellular ROS and reduce the mitochondrial membrane potential, arrest the cell cycle in the S-phase, and induce DNA damage, eventually leading to autophagy. The expression level of phosphorylated STAT3 and STAT3-related cyclin D1 were obviously down-regulated in MCF-7 cells after being treated with **Ir-PTS-4**. The cell metastasis and invasion were also inhibited after **Ir-PTS-4** treatment. **Ir-PTS-4** also exhibited excellent anti-proliferation activity in 3D multicellular tumor spheroids, suggesting the potential to inhibit solid tumors *in vivo*. The combination of PTS-derived ligand with iridium-based metal complex presents the rational design of metal-based anticancer agents to block STAT3 pathway for simultaneously inhibiting tumor proliferation and metastasis.

CRediT authorship contribution statement

Yan Su: Investigation, Writing – original draft. **Jin Yang:** Investigation. **Meng-Meng Wang:** Investigation. **Hong-Bao Fang:** Supervision, Funding acquisition. **Hong-Ke Liu:** Supervision, Funding acquisition. **Zheng-Hong Yu:** Supervision, Funding acquisition. **Zhi Su:** Writing – original draft, Supervision, Funding acquisition.

Declaration of Competing Interest

The authors declare that they have no known competing financial interests or personal relationships that could have appeared to influence the work reported in this paper.

Data availability

Data will be made available on request.

Acknowledgments

We appreciate the financial support from the National Natural Science Foundation of China (NSFC) (Grant No. 21977052, 22077066) and Distinguished Young Scholars of Jiangsu Province (BK20230006). Y. Su was supported by the Jiangsu Excellent Postdoctoral Program and NSF of Jiangsu Province (BK20231090).

Appendix A. Supplementary data

Supplementary data to this article can be found online at https://doi.org/10.1016/j.jinorgbio.2023.112427.

References

[1] R.L. Siegel, K.D. Miller, H.E. Fuchs, A. Jemal, Cancer statistics, 2021, CA Cancer J. Clin. 71 (2021) 7–33.
[2] C.L. Chaffer, R.A. Weinberg, A perspective on cancer cell metastasis, Science 331 (2011) 1559–1564.
[3] L. Yang, P. Shi, G. Zhao, J. Xu, W. Peng, J. Zhang, G. Zhang, X. Wang, Z. Dong, F. Chen, H. Cui, Targeting cancer stem cell pathways for cancer therapy, Signal Transduct. Target. Ther. 5 (2020) 8.
[4] J. Huynh, A. Chand, D. Gough, M. Ernst, Therapeutically exploiting STAT3 activity in cancer - using tissue repair as a road map, Nat. Rev. Cancer 19 (2019) 82–96.
[5] K.S. Siveen, S. Sikka, R. Surana, X. Dai, J. Zhang, A.P. Kumar, B.K.H. Tan, G. Sethi, A. Bishayee, Targeting the STAT3 signaling pathway in cancer: role of synthetic and natural inhibitors, Biochim. Biophys. Acta 2014 (1845) 136–154.
[6] H. Yu, H. Lee, A. Herrmann, R. Buettner, R. Jove, Revisiting STAT3 signalling in cancer: new and unexpected biological functions, Nat. Rev. Cancer 14 (2014) 736–746.
[7] C.P. Tan, Y.Y. Lu, L.N. Ji, Z.W. Mao, Metallomics insights into the programmed cell death induced by metal-based anticancer compounds, Metallomics 6 (2014) 978–995.
[8] L. Feng, Y. Geisselbrecht, S. Blanck, A. Wilbuer, G.E. Atilla-Gokcumen, P. Filippakopoulos, K. Kraling, M.A. Celik, K. Harms, J. Maksimoska, R. Marmorstein, G. Frenking, S. Knapp, L.O. Essen, E. Meggers, Structurally sophisticated octahedral metal complexes as highly selective protein kinase inhibitors, J. Am. Chem. Soc. 133 (2011) 5976–5986.
[9] A.G. Quiroga, C. Navarro Ranninger, Contribution to the SAR field of metallated and coordination complexes, Coord. Chem. Rev. 248 (2004) 119–133.
[10] D.-L. Ma, L.-J. Liu, K.-H. Leung, Y.-T. Chen, H.-J. Zhong, D.S.-H. Chan, H.-M. D. Wang, C.-H. Leung, Antagonizing STAT3 dimerization with a rhodium(III) complex, Angew. Chem. Int. Ed. 53 (2014) 9178–9182.
[11] T.-S. Kang, W. Wang, H.-J. Zhong, Z.-Z. Dong, Q. Huang, S.W.F. Mok, C.-H. Leung, V.K.W. Wong, D.-L. Ma, An anti-prostate cancer benzofuran-conjugated iridium (III) complex as a dual inhibitor of STAT3 and NF-κB, Cancer Lett. 396 (2017) 76–84.
[12] F. Porta, G. Facchetti, N. Ferri, A. Gelain, F. Meneghetti, S. Villa, D. Barlocco, D. Masciocchi, A. Asai, N. Miyoshi, S. Marchianò, B.-M. Kwon, Y. Jin, V. Gandin, C. Marzano, I. Rimoldi, An in vivo active 1,2,5-oxadiazole Pt(II) complex: a promising anticancer agent endowed with STAT3 inhibitory properties, Eur. J. Med. Chem. 131 (2017) 196–206.
[13] J. Zang, B. Zhang, Y. Wang, X. Wang, S. Gou, Design, synthesis and biological evaluation of antitumor platinum(II) agents conjugated with non-steroidal anti-inflammatory drug species, Bioorg. Chem. 120 (2022), 105633.
[14] L. Cai, Y. Wang, H. Chen, Y. Tan, T. Yang, S. Zhang, Z. Guo, X. Wang, Platinum(IV) complexes as inhibitors of STAT3 and regulators of the tumor microenvironment to control breast cancer, J. Med. Chem. 66 (2023) 11351–11364.
[15] M. Ali Nazif, J.A. Bangert, I. Ott, R. Gust, R. Stoll, W.S. Sheldrick, Dinuclear organoiridium(III) mono- and bis-intercalators with rigid bridging ligands: synthesis, cytotoxicity and DNA binding, J. Inorg. Biochem. 103 (2009) 1405–1414.
[16] Z. Liu, A. Habtemariam, A.M. Pizarro, S.A. Fletcher, A. Kisova, O. Vrana, L. Salassa, P.C. Bruijnincx, G.J. Clarkson, V. Brabec, P.J. Sadler, Organometallic half-sandwich iridium anticancer complexes, J. Med. Chem. 54 (2011) 3011–3026.
[17] J. Ruiz, V. Rodriguez, N. Cutillas, K.G. Samper, M. Capdevila, O. Palacios, A. Espinosa, Novel C,N-chelate rhodium(III) and iridium(III) antitumor complexes incorporating a lipophilic steroidal conjugate and their interaction with DNA, Dalton Trans. 41 (2012) 12847–12856.
[18] A. Wilbuer, D.H. Vlecken, D.J. Schmitz, K. Kraling, K. Harms, C.P. Bagowski, E. Meggers, Iridium complex with antiangiogenic properties, Angew. Chem. Int. Ed. 49 (2010) 3839–3842.
[19] C. Kunick, I. Ott, Metal complexes as protein kinase inhibitors, Angew. Chem. Int. Ed. 49 (2010) 5226–5227.
[20] Z. Ma, X. Zhang, L. Xu, D. Liu, S. Di, W. Li, J. Zhang, H. Zhang, X. Li, J. Han, X. Yan, Pterostilbene: mechanisms of its action as oncostatic agent in cell models and in vivo studies, Pharmacol. Res. 145 (2019), 104265.
[21] Y. Li, X. Qiang, Y. Li, X. Yang, L. Luo, G. Xiao, Z. Cao, Z. Tan, Y. Deng, Pterostilbene-O-acetamidoalkylbenzylamines derivatives as novel dual inhibitors of cholinesterase with anti-beta-amyloid aggregation and antioxidant properties for the treatment of Alzheimer's disease, Bioorg. Med. Chem. Lett. 26 (2016) 2035–2039.
[22] Q. Wu, K.Y. Zhang, P. Dai, H. Zhu, Y. Wang, L. Song, L. Wang, S. Liu, Q. Zhao, W. Huang, Bioorthogonal "labeling after recognition" affording an FRET-based luminescent probe for detecting and imaging Caspase-3 via photoluminescence lifetime imaging, J. Am. Chem. Soc. 142 (2020) 1057–1064.
[23] B.B. Chen, N.L. Pan, J.X. Liao, M.Y. Huang, D.C. Jiang, J.J. Wang, H.J. Qiu, J. X. Chen, L. Li, J. Sun, Cyclometalated iridium(III) complexes as mitochondria-targeted anticancer and antibacterial agents to induce both autophagy and apoptosis, J. Inorg. Biochem. 219 (2021), 111450.
[24] C. Fu, Q. Lv, J. Fan, S. Wu, M. Lei, X. Zhang, X. Li, W. Zhou, Y. Yu, W. Ren, C. Zhao, G. Liao, Discovery of polypyridyl iridium(III) complexes as potent agents against resistant Candida albicans, Eur. J. Med. Chem. 233 (2022), 114250.
[25] B. Wang, T. Liu, Z. Wu, L. Zhang, J. Sun, X. Wang, Synthesis and biological evaluation of stilbene derivatives coupled to NO donors as potential antidiabetic agents, J. Enzyme Inhib. Med. Chem. 33 (2018) 416–423.
[26] M.-M. Wang, F.-J. Xu, Y. Su, Y. Geng, X.-T. Qian, X.-L. Xue, Y.-Q. Kong, Z.-H. Yu, H.-K. Liu, Z. Su, A new strategy to fight metallodrug resistance: mitochondria-relevant treatment through mitophagy to inhibit metabolic adaptations of cancer cells, Angew. Chem. Int. Ed. 61 (2022), e202203843.
[27] R.-R. Ye, B.-C. Chen, J.-J. Lu, X.-R. Ma, R.-T. Li, Phosphorescent rhenium(I) complexes conjugated with artesunate: mitochondrial targeting and apoptosis-ferroptosis dual induction, J. Inorg. Biochem. 223 (2021), 111537.
[28] Y. Su, H. Lin, Y. Tu, M.-M. Wang, G.-D. Zhang, J. Yang, H.-K. Liu, Z. Su, Fighting metallodrug resistance through alteration of drug metabolism and blockage of autophagic flux by mitochondria-targeting AIEgens, Chem. Sci. 13 (2022) 1428–1439.
[29] R.R. Ye, C.P. Tan, M.H. Chen, L. Hao, L.N. Ji, Z.W. Mao, Mono- and dinuclear phosphorescent rhenium(I) complexes: impact of subcellular localization on anticancer mechanisms, Chemistry 22 (2016) 7800–7809.
[30] L. Xu, P.P. Zhang, X.Q. Fang, Y. Liu, J.Q. Wang, H.Z. Zhou, S.T. Chen, H. Chao, A ruthenium(II) complex containing a p-cresol group induces apoptosis in human cervical carcinoma cells through endoplasmic reticulum stress and reactive oxygen species production, J. Inorg. Biochem. 191 (2019) 126–134.
[31] R.V. Rao, H.M. Ellerby, D.E. Bredesen, Coupling endoplasmic reticulum stress to the cell death program, Cell Death Differ. 11 (2004) 372–380.

[32] Y. Liu, Y. Ye, Proteostasis regulation at the endoplasmic reticulum: a new perturbation site for targeted cancer therapy, Cell Res. 21 (2011) 867–883.
[33] B. Yuan, J. Liu, R. Guan, C. Jin, L. Ji, H. Chao, Endoplasmic reticulum targeted cyclometalated iridium(iii) complexes as efficient photodynamic therapy photosensitizers, Dalton Trans. 48 (2019) 6408–6415.
[34] D. Trachootham, J. Alexandre, P. Huang, Targeting cancer cells by ROS-mediated mechanisms: a radical therapeutic approach? Nat. Rev. Drug Discov. 8 (2009) 579–591.
[35] C.P. LeBel, H. Ischiropoulos, S.C. Bondy, Evaluation of the probe 2′,7′-dichlorofluorescin as an indicator of reactive oxygen species formation and oxidative stress, Chem. Res. Toxicol. 5 (1992) 227–231.
[36] M. Xia, Y. Zhang, K. Jin, Z. Lu, Z. Zeng, W. Xiong, Communication between mitochondria and other organelles: a brand-new perspective on mitochondria in cancer, Cell Biosci. 9 (2019) 27.
[37] M. Redmann, M. Dodson, M. Boyer-Guittaut, V. Darley-Usmar, J. Zhang, Mitophagy mechanisms and role in human diseases, Int. J. Biochem. Cell Biol. 53 (2014) 127–133.
[38] T. Kanki, K. Furukawa, S. Yamashita, Mitophagy in yeast: molecular mechanisms and physiological role, Biochim. Biophys. Acta 2015 (1853) 2756–2765.
[39] J. Kim, M. Kundu, B. Viollet, K.L. Guan, AMPK and mTOR regulate autophagy through direct phosphorylation of Ulk1, Nat. Cell Biol. 13 (2011) 132–141.
[40] Q.P. Liang, T.Q. Xu, B.L. Liu, X.P. Lei, J.R. Hambrook, D.M. Zhang, G.X. Zhou, Sasanquasaponin IotaIotaIota from Schima crenata Korth induces autophagy through Akt/mTOR/p70S6K pathway and promotes apoptosis in human melanoma A375 cells, Phytomedicine 58 (2019), 152769.
[41] G.L. Wong, S.G. Manore, D.L. Doheny, H.-W. Lo, STAT family of transcription factors in breast cancer: pathogenesis and therapeutic opportunities and challenges, Semin. Cancer Biol. 86 (2022) 84–106.
[42] S. Zou, Q. Tong, B. Liu, W. Huang, Y. Tian, X. Fu, Targeting STAT3 in cancer immunotherapy, Mol. Cancer 19 (2020) 145.
[43] S. Li, W. Zhang, Y. Yang, T. Ma, J. Guo, S. Wang, W. Yu, L. Kong, Discovery of oral-available resveratrol-caffeic acid based hybrids inhibiting acetylated and phosphorylated STAT3 protein, Eur. J. Med. Chem. 124 (2016) 1006–1018.
[44] C.S. Shin, B. Kwak, B. Han, K. Park, Development of an in vitro 3D tumor model to study therapeutic efficiency of an anticancer drug, Mol. Pharm. 10 (2013) 2167–2175.